Nanoscale Horizons

ROYAL SOCIETY OF CHEMISTRY

COMMUNICATION

View Article Online
View Journal | View Issue

Cite this: *Nanoscale Horiz.*, 2025, **10**, 2986

Received 14th February 2025, Accepted 24th June 2025

DOI: 10.1039/d5nh00089k

rsc.li/nanoscale-horizons

Modulation of photoluminescence in a MoS_2 device through tuning the quantum tunneling effect

Bor-Wei Liang,*[a] Ruei-Yu Hsu,[b] Wen-Hao Chang,[b] Ye-Ru Chen,[b] You-Jia Huang,[b] Tilo H. Yang,[c] Yu Liang Li,[a] Chin-Yuan Su,[d] Ting-Hua Lu[b] and Yann-Wen Lan*[b]

Transition metal dichalcogenide (TMD) materials, such as molybdenum disulfide (MoS_2), have emerged as promising platforms for exploring electrically tunable light–matter interactions, which are critical for designing high-performance photodetector systems. In this study, we investigate the advancements in quantum tunneling MoS_2 field-effect transistors (QT-MoS_2 FETs) and their optoelectronic properties, with a focus on photoresponse behavior and photoluminescence (PL) spectral variations driven by photoinduced tunneling currents through oxide layers. The results demonstrate that tunneling-induced exciton and trion dissociation effects lead to a pronounced blue shift in PL spectral peaks and significant changes in light intensity. Compared to normal MoS_2 FETs, QT-MoS_2 FETs exhibit considerably enhanced PL spectral modulation under applied gate bias, underscoring the critical role of tunneling currents in governing optical responses. This work advances the understanding of 2D material-based optoelectronics and highlights their potential for next-generation photodetector applications.

New concepts

This work introduces a quantum tunneling-based strategy to modulate photoluminescence (PL) in monolayer MoS_2 field-effect transistors (FETs) by leveraging trap-assisted tunneling currents across defective gate dielectrics. Unlike conventional gate-tuned PL modulation approaches, which rely on lateral carrier transport and high gate voltages, our method utilizes vertical tunneling currents to directly influence excitonic states, enabling highly efficient and reversible modulation of exciton behavior at significantly lower operating voltages. This approach marks a departure from prior studies that required nanoscale probe-induced tunneling or relied solely on electrostatic doping with high electrical field. Our device-level demonstration showcases how engineered tunneling pathways can serve as an active mechanism for exciton control, leading to large PL intensity shifts and excitonic peak blue-shifts under moderate gate bias. This concept provides new insight into the role of vertical tunneling in 2D optoelectronics and highlights a previously underexplored mechanism for excitonic modulation. The findings pave the way toward scalable exciton-based quantum tunneling devices such as optical logic circuits, valleytronic switches, and sensitive photonic sensors, offering a new direction for integrating quantum tunneling effects into next-generation optoelectronic and quantum communication platforms.

Introduction

Two-dimensional (2D) transition metal dichalcogenides (TMD) materials, such as MoS_2, have been investigated as channel materials for n-type field effect transistors (FET) due to their nanometer-scale thickness and ultra-low contact resistance when interfaced with semimetal contacts.[1–4] The intrinsic two-dimensionality of TMDs confines carriers within the layer, promoting robust quantum confinement and strong electron–electron or electron–hole Coulomb interactions.[5–8] These characteristics distinguish TMD-based FETs from their traditional bulk semiconductor counterparts, enabling unique optical phenomena such as excitons, trions, and broadband optical absorption, alongside spin–valley polarized excitations.[9–13] The distinct electrical and optical properties of TMDs present new opportunities for heterogeneous integration, paving the way for their application in next-generation MOSFETs, tunneling photodiodes, and polarization-sensitive sensors.[14–20]

Excitonic properties studies on TMD FET devices offer the capability to modulate free carrier densities—both electrons and holes—for a given exciton population, which can be further tailored *via* electrostatic doping strategies and enable electrically tunable light absorption and photoluminescence (PL) spectra, providing a foundation for the development of nanoscale electro-optical modulators.[21,22] However, conventional gate-tuned PL modulation techniques, which rely on lateral carrier transport in standard FET architectures, impose

[a] *Institute of Electro-Optical Engineering, National Taiwan Normal University, Taipei 11677, Taiwan. E-mail: bwliang@ntnu.edu.tw*
[b] *Department of Physics, National Taiwan Normal University, Taipei 11677, Taiwan. E-mail: ywlan@ntnu.edu.tw*
[c] *Department of Electrical Engineering and Computer Science, Massachusetts Institute of Technology, Cambridge, Massachusetts, USA*
[d] *Graduate Institute of Energy Engineering, National Central University, Taoyuan, Taiwan*

significant limitations. These approaches typically require the application of high electric fields across the TMD channel, restricting the efficiency and performance of such devices in exciton-based modulation applications.[23]

The excitonic properties of TMD-based optoelectronic devices can be significantly altered by the vertical carrier transport mechanism.[24–27] The defects in gate dielectric can lead to a substantial increase in carrier tunneling through the oxide layer to the TMD channel due to electrostatic or thermal effects.[28] In another case, under controlled conditions, layer-to-layer tunneling currents through the TMD material can also be harnessed as a functional mechanism in van der Waals heterostructure devices.[17,20,29] Such vertical tunneling currents, induced by external electric fields, can profoundly influence the optoelectronic properties of TMD-based phototransistors. For instance, changes in exciton or trion dissociation induced by strong electric fields can be directly observed through photocurrent measurements, as photocurrent generation originates from the conversion of excitons into free carriers.[30] Theoretical studies suggest that strong electric fields can provide sufficient energy for efficient exciton dissociation, thereby modifying the absorption and emission characteristics of TMD devices.[6,31,32] Consequently, two-dimensional materials are highly sensitive to spectral response variations under vertical and lateral electric fields or carrier flows. The high trap density in the gate dielectric of MoS_2 FETs can induce photoinduced tunneling currents and alter the gate voltage drop across the MoS_2 channel, leading to significant differences in PL spectra intensity and peak positions as the applied voltage varies. Therefore, in contrast to conventional gate-tuned PL modulation approaches that rely on lateral carrier transport in FET architectures, quantum tunneling-based electronics is presented for directly modulating exciton dynamics in 2D TMDs. This tunneling-driven mechanism enables significantly enhanced PL modulation compared to traditional electrostatic gating with lower operating voltages.

In this study, we fabricated quantum tunneling MoS_2 FETs (QT-MoS_2 FETs) featuring a high trap density gate oxide layer that facilitates tunneling photocurrents and examined their photoresponse properties. Moreover, we investigated the variations in the PL spectra of the MoS_2 channel under different gate voltages. The steady-state PL spectra revealed the formation of A-excitons in the MoS_2 monolayer, with a notably stronger excitonic photoresponse attributed to the trap-assisted (TA) tunneling. While prior studies have observed tunneling-induced excitonic modulation using scanning probe techniques at the nanoscale,[33] our work advances this concept by demonstrating device-level control, achieving gate-controlled excitonic modulation suitable for practical valleytronic applications. The demonstrated capability for reversible and dynamic control over excitonic properties highlights the potential of this platform for integration into future quantum photonic and optoelectronic systems.

Results and discussion

To compare FET behaviors, we separately fabricated two kinds of MoS_2 field-effect transistors (FET) on a hBN/SiO_2/Si substrate and a SiO_2/Si substrate, respectively, where the oxides acted as gate dielectrics and the heavily-doped Si was used as a back gate. The schematic of the quantum tunneling MoS_2 field-effect transistor (QT-MoS_2 FET) and representative optical microscopy (OM) image are depicted in Fig. 1a and b, respectively. The area of the monolayer MoS_2 material is indicated by dashed lines. The MoS_2 layer, synthesized on a sapphire substrate *via* chemical vapor deposition (CVD), was transferred onto P^{++} Si substrates ($N_a \sim 10^{19}$ cm^{-3}) with SiO_2 (30 nm) layers acting as the back gate dielectric (see Methods section for details). Fig. S1a presents the AFM image of 0.85 nm MoS_2 transferred onto a SiO_2 substrate, while Fig. S1b displays the corresponding Raman spectra. The absence of any apparent artificial cracks suggests that the transfer conditions employed are well-suited for maintaining the structural integrity and quality of the MoS_2 monolayer. 5 nm hBN was also transferred onto SiO_2 using PMMA to reduce the interface defects between MoS_2 and SiO_2, thereby decreasing the electrical hysteresis effects and interface charge between MoS_2 and the gate dielectric of the QT-MoS_2 FET (see Fig. S2). The source/drain electrodes were Bi (20 nm) and Au (40 nm) patterned with electron beam lithography and deposited using a thermal evaporator. After FET fabrication, we used wire bonding on the outside probe pad to break down the thin oxide layer, allowing carriers to tunnel through the defects and pass through the oxide layer.

The characteristic drain current ($I_{DS,dark}$, solid line) and gate current ($I_{GS,dark}$, dash line) under dark conditions *versus* gate voltage (V_{GS}) curves of QT-MoS_2 FET are shown in Fig. 1c. Fig. 1d is log scale of Fig. 1c. The QT-MoS_2 FET exhibits unipolar n-type behavior with a high on/off current ratio of 10^4 at V_{DS} = −1 V and the V_{GS} range = ±2 V. The values of I_{GS} and I_{DS} in the QT-MoS_2 FETs are similar but opposite, which means that the leakage I_{GS} current dominates the FET device's current. This suggests that, during the wire bonding process, high-voltage pulses cause a high density of defects within the hBN and SiO_2 gate dielectric layer, and these defects form

Yann-Wen Lan

Over the past eight years in academia, I've had the privilege of publishing seven papers—including this invited contribution—in Nanoscale Horizons. It has felt like growing alongside the journal, with nearly one article each year. For this special 10th anniversary issue, we align our work with the upcoming 2025 Quantum Year, exploring how quantum effects modulate the behavior of two-dimensional optoelectronic devices. Through this, we celebrate Nanoscale Horizons and wish the journal continued success as it leads the way at the forefront of scientific discovery.

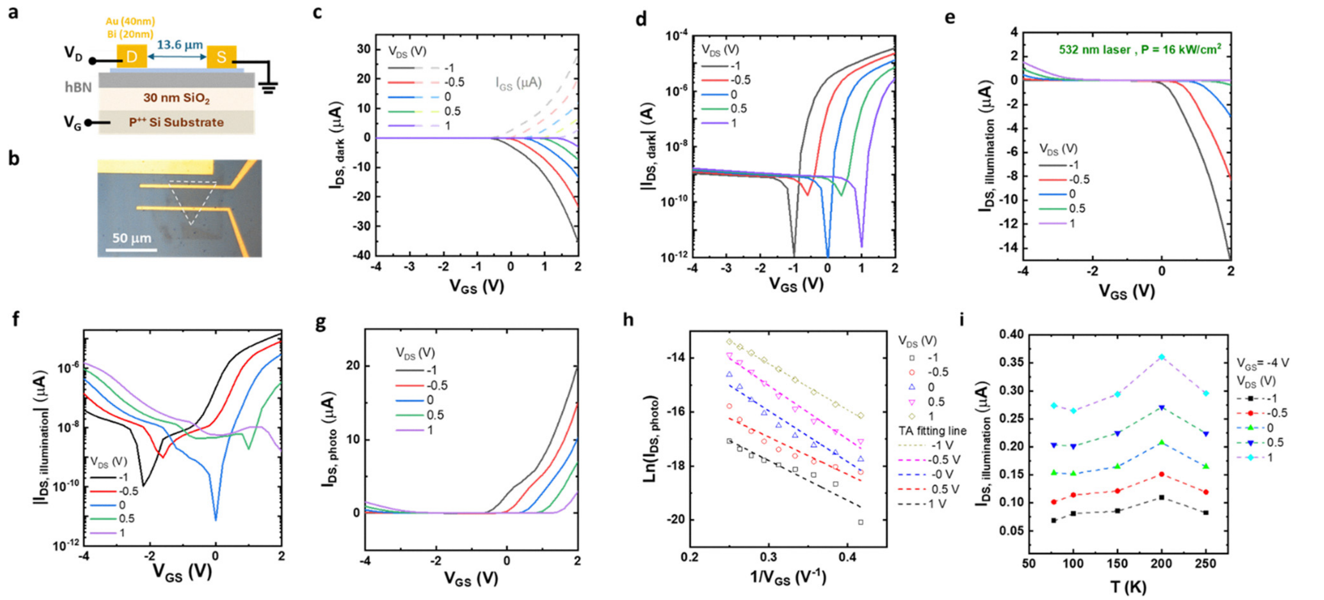

Fig. 1 Performance of the QT-MoS_2 FET. (a) Schematic diagram and (b) the OM image of the QT-MoS_2 FET device. The MoS_2 channel is a monolayer. (c) Output characteristics (I_{DS}–V_{GS}) of the device, and (d) the log scale electrical properties under dark conditions. (e) Output characteristics ($I_{DS,illumination}$–V_{GS}) of the QT-MoS_2 device under green laser illumination and (f) the log scale electrical properties under green laser illumination. (g) The photocurrent ($I_{DS,photo} = I_{DS,illumination} - I_{DS,Dark}$) characteristic of QT-$MoS_2$. (h) Linear fitting of TA tunneling for the output characteristics ($I_{DS,photo}$–V_{GS}) of the QT-MoS_2 device under green laser illumination. (i) Temperature-dependent $I_{DS,illumination}$–V_{GS} measurements with varying V_{DS}, recorded from T = 75 K to T = 250 K.

conductive channels, allowing the oxide layer to lose its blocking effect on the gate terminal and create a pathway. As MoS_2 is an n-type semiconductor, under negative gate bias ($V_{GS} < 0$) in dark conditions, the intrinsic hole concentration is insufficient to support a significant tunneling current. However, under illumination, electron–hole pairs are generated. While the electrons are efficiently swept away, the holes accumulate at the MoS_2/gate dielectric interface, creating a built-in electric field that surpasses the turn-on threshold. This facilitates carrier tunneling through the hBN/SiO_2 dielectric layers *via* trap states, which in turn governs the behavior of the QT-MoS_2 FET at $V_{GS} < 0$. Similar observations of hole accumulation in n-type semiconductors have been reported, such as in the gr/SiN/n-Si diode structure.[34]

Fig. 1e shows the illumination-induced drain–source current $I_{DS,illumination}$–V_{GS} characteristics after illuminating the QT-MoS_2 FET with a 532 nm laser. Fig. 1f is the log scale of Fig. 1e. The laser is focused onto a spot with a diameter of 2 μm and the laser power is 0.51 mW. The intensity (P) is about 16 kW cm^{-2}. It can be observed that under 532 nm laser illumination, the $I_{DS,illumination}$–V_{GS} characteristics of the QT-MoS_2 FET exhibit ambipolar behavior. When a negative gate bias ($V_{GS} < 0$ V) is applied, the $I_{DS,illumination}$ increases dramatically—from the nanoampere level observed in the dark (see Fig. 1d) to the microampere scale—indicating that the photoresponse is governed by tunneling-dominated mechanisms. In contrast, under positive gate bias, the $I_{DS,illumination}$ remains in the microampere range and closely resembles the dark current, suggesting minimal photoinduced enhancement. Under dark conditions, the QT-MoS_2 FET exhibits unipolar n-type characteristics; a negative V_{GS} depletes electrons in the MoS_2 channel, effectively switching off the device and suppressing the I_{DS}. However, upon illumination with a 532 nm laser, the negative gate bias modulates the energy band profile of the hBN/SiO_2 stack and makes the carriers tunnel through the gate dielectric. The photoexcited holes gain sufficient energy to tunnel through the oxide traps embedded within the dielectric, enabling a trap-assisted tunneling photocurrent from the MoS_2 channel to the P^{++} Si substrate. This results in a photocurrent that is several orders of magnitude larger than the dark current, as shown in Fig. 1c. This behavior demonstrates a dual transport regime—electron conduction at $V_{GS} > 0$ V and hole-assisted tunneling at $V_{GS} < 0$ V—leading to ambipolar I_{DS}–V_{GS} characteristics in the QT-MoS_2 FET.

Fig. 1g presents the characteristic curve of the photocurrent ($I_{DS,photo} = I_{DS,illumination} - I_{DS,dark}$) against V_{GS}. It is evident that $I_{DS,photo}$ is positive regardless of whether V_{DS} is positive or negative, indicating that the direction of the photocurrent is primarily from the holes provided by MoS_2 towards the P^{++} Si side. The photoinduced carrier transport mechanism between the MoS_2 channel and the P^{++} Si gate electrode in the QT-MoS_2 FET is verified through TA tunneling fitting of $I_{DS,photo}$, as shown in Fig. 1h. The results exhibit a strong agreement with the TA tunneling mechanism in the gate voltage range of -4 V $< V_{GS} < -1$ V, as confirmed by the linear behavior observed in the ln(I) *versus* V^{-1} plot at various V_{GS} values.[35] Notably, all R^2 values exceed 0.88, further indicating that TA tunneling is the dominant mechanism governing the photocurrent under these bias conditions. Furthermore, temperature-dependent measurements of I_{DS} under illumination, conducted from 78 K to 250 K (Fig. 1i), reveal nearly constant current levels across varying temperatures at fixed V_{DS} values, supporting that the tunneling of photoexcited carriers from the MoS_2 channel to the P^{++} Si gate electrode is the primary contributor to the photocurrent generation. This fitting result confirms that, under laser illumination, carriers originating from the MoS_2 channel can undergo stepwise tunneling through a series of defect-induced trap states within the SiO_2/hBN dielectric stack. This trap-assisted mechanism enables the flow of photoinduced current, under moderate bias conditions.

To compare with the QT-MoS_2 FET behavior, we fabricated and demonstrated a normal MoS_2 FET on a SiO_2 (100 nm)/P^{++} Si substrate, where the thicker oxide layer effectively prevents leakage current between the source and gate terminals (see Fig. 2a and b). The electrical characteristics of the normal MoS_2 FET show distinct differences compared to those of the QT-MoS_2 FET. As depicted in Fig. 2c and d, the $I_{DS,dark}$ *versus* V_{GS} curves for the normal MoS_2 FET under dark conditions show that $I_{DS,dark}$ approaches zero when no transverse field is applied to the MoS_2 channel (V_{DS} = 0 V) over the range of −20 V < V_{GS} < 20 V. Fig. 2e shows the I_{GS}–V_{GS} characteristics of the normal MoS_2 FET. The leakage current (I_{GS}) in the normal MoS_2 device is approximately 1 nA—significantly lower than the μA-level leakage observed in the QT-MoS_2 FET. This suggests that, unlike in the QT-MoS_2 FET, the current from the gate terminal (that is I_{GS}) does not dominate the overall output current flowing to the drain terminal. Even at high V_{GS} values (∼20 V), the 100 nm-thick SiO_2 layer effectively blocks electrons from the P^{++} Si gate, preventing leakage current through the gate dielectric. The normal MoS_2 FET exhibits typical n-type channel behavior. When the device is illuminated with a focused laser beam (16 kW cm^{-2}) at varying V_{DS} biases, the $I_{DS,illumination}$–V_{GS} and $I_{DS,photo}$–V_{GS} characteristics show that the OFF current increases to the μA range (see Fig. 2f and g). This indicates that the photocurrent in the normal MoS_2 FET is dominated by photogenerated carriers in the MoS_2 channel across the entire operating range of the device, unlike the QT-MoS_2 FET, where the tunneling current formed between the high-defect SiO_2/hBN and MoS_2 layers plays a dominant role.

Fig. 3a shows the band diagram from the drain to the gate under dark conditions when V_{DS} = 0 V and V_{GS} < 0 V. At V_{GS} < 0 V, the energy bands of the P^{++} silicon substrate shift downwards, increasing the barrier height for the holes, which reduces the leakage current between the gate and the channel. Within the MoS_2 channel of the FET, electrons are repelled from the MoS_2/hBN interface to establish a depletion layer, reducing the carrier concentration in the n-type MoS_2 channel. Further increasing the negative V_{GS} would create an inversion channel by negative charge induced by the SiO_2 gate dielectric. Therefore, the carriers within the MoS_2 channel are predominantly holes. The band diagram of the QT-MoS_2 FET under laser illumination is shown in Fig. 3b. At this time, the photons from the laser light excited the hole carriers between the MoS_2

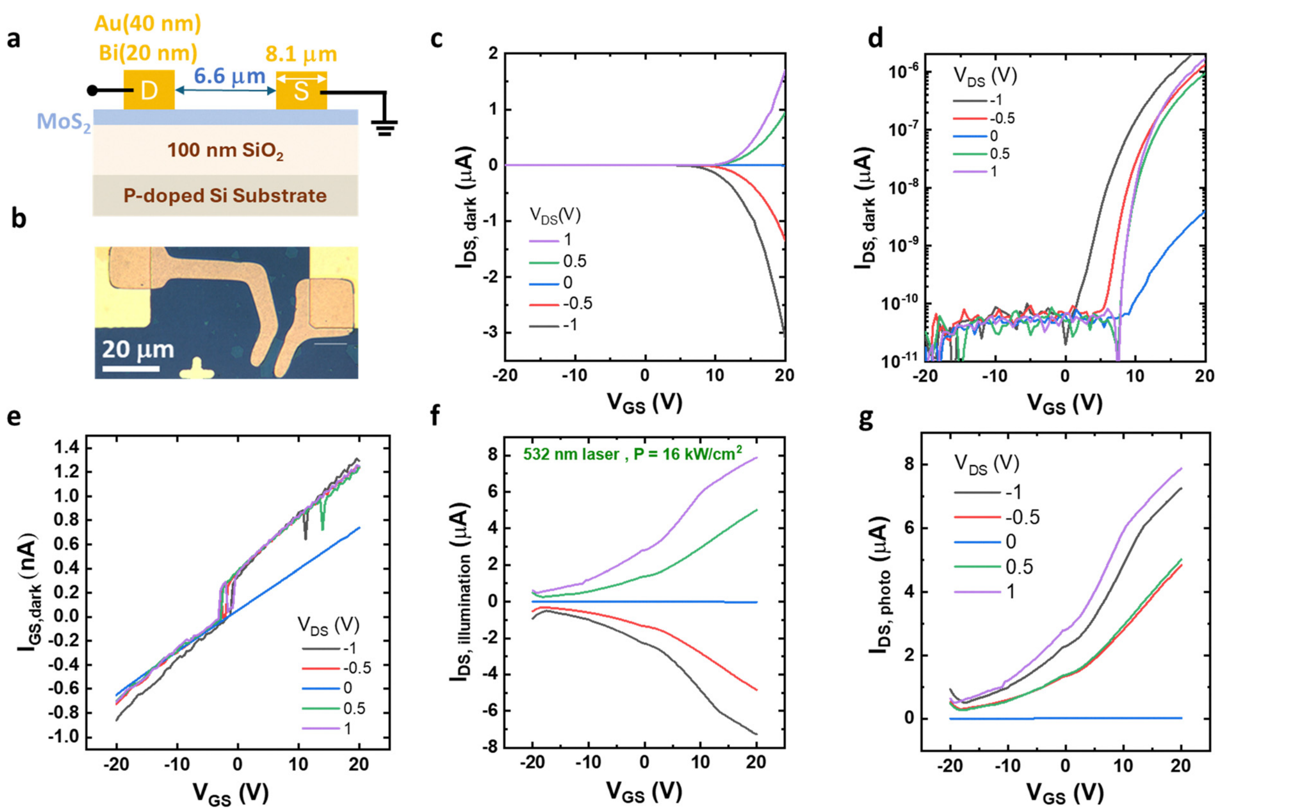

Fig. 2 Performance of the normal MoS_2 FET. (a) Schematic diagram and (b) the OM image of the normal MoS_2 FET device. (c) Output characteristics (I_{DS}–V_{GS}) of the normal MoS_2 FET device, and (d) the log scale electrical properties under dark condition. (e) The I_{GS}–V_{GS} characteristics of the normal MoS_2 FET. (f) Output characteristics ($I_{DS,illumination}$–V_{GS}) of the normal MoS_2 FET device under green laser illumination. (g) The photocurrent ($I_{DS,photo}$= |$I_{DS,illumination}$ − $I_{DS,Dark}$|) characteristic.

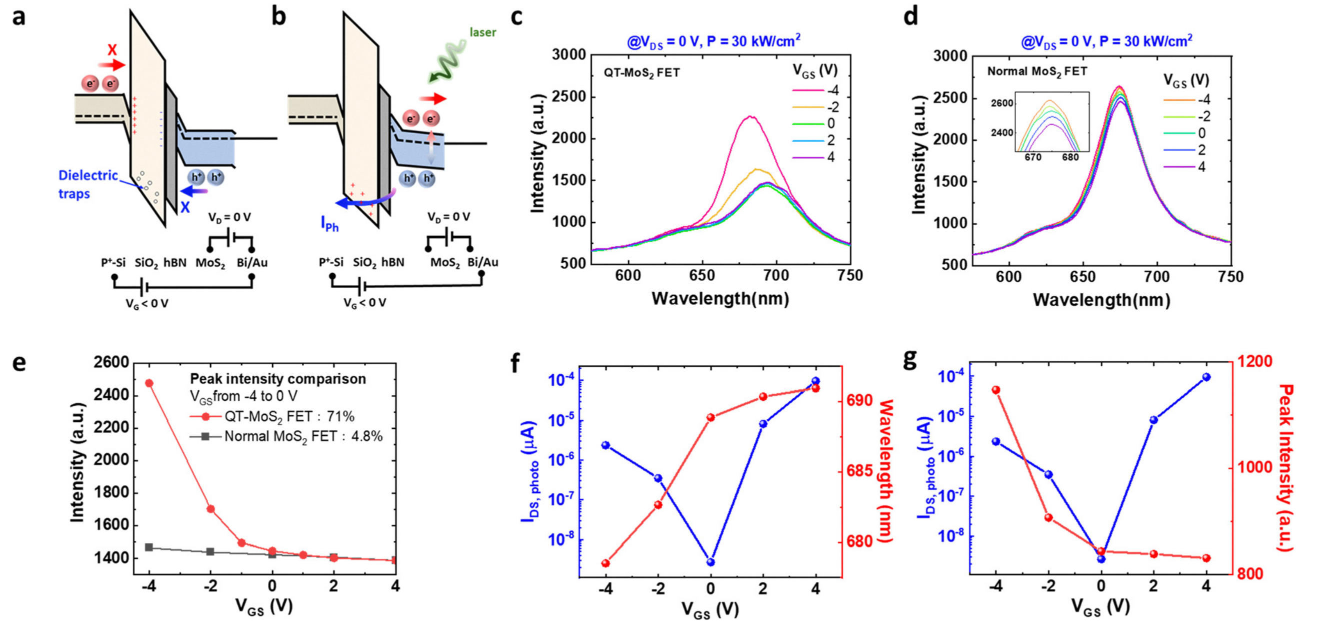

Fig. 3 Photoluminescence (PL) characteristics of QT-MoS_2 FETs under different gate biases. (a) Energy band diagram of the QT-MoS_2 FET under dark conditions. (b) Energy band diagram of the QT-MoS_2 FET under 532 nm laser illumination. The laser intensity is 30 kW cm^{-2}. (c) PL spectra of the QT-MoS_2 FET as a function of applied V_{GS}. (d) PL spectra of the normal MoS_2 FET modulated by different V_{GS} values. (e) Comparison of the PL peak intensity of the QT-MoS_2 FET at various V_{GS} values. (f) Photocurrent ($I_{DS,photo}$) and PL peak position of the QT-MoS_2 FET as a function of V_{GS}. (g) Photocurrent ($I_{DS,photo}$) and PL peak intensity of the QT-MoS_2 FET as a function of applied V_{GS}.

and hBN layers, causing the hole carriers to undergo TA tunneling through the hBN and SiO_2 tunneling barriers to the gate terminal, forming a photocurrent (I_{ph}) and fixed oxide charge in SiO_2. When V_{DS} increases, more electrons are moved out of the MoS_2/hBN at the drain end, resulting in more holes at the drain end. On the other hand, the photocurrent through MoS_2 and SiO_2 will cause a redistribution of charges and bias, leading to a reduced portion of the V_{GS} voltage drop being sustained by SiO_2, thus subjecting MoS_2 to a larger longitudinal voltage drop. This phenomenon will result in changes to the spectral characteristics of the 2D material.

After understanding the differences in current generation mechanisms between the QT-MoS_2 FET and normal MoS_2 FET, the next step is to observe the spectral changes under applied bias. The PL spectrum measurements for the QT-MoS_2 FET were conducted under a 532 nm green laser with a fixed V_{DS} of 0 V, simultaneously measuring the PL spectrum and the corresponding electrical characteristics at different V_{GS}. The applied laser intensity on the devices was 30 kW cm^{-2}. Fig. 3c shows the PL spectra of the QT-MoS_2 FET with varying V_{GS}. Measurements were taken with V_{GS} ranging from −4 V to 4 V in 2 V increments. It can be seen that the PL intensity decreases with increasingly positive V_{GS}. Similar trends are observed for the normal MoS_2 FET, but the change in PL intensity is much smaller compared to the QT-MoS_2 FET under varying applied V_{GS} bias (see Fig. 3d).

The relationship between photocurrent, PL intensity, and V_{GS}. It can be observed that the trend of increasing peak intensity matches the trend of increasing tunneling photocurrent. Notice that when $V_{GS} < 0$ V, the higher the tunneling photocurrent, the stronger the PL intensity. Additionally, the rapid increase in PL intensity occurs at the same onset voltage where tunneling happens, which is at $V_{GS} < -2$ V. Note that the PL peak position reveals that V_{DS} is kept at 0 V during the measurements, so the photocurrent flows from the drain to the gate. Unlike the traditional exciton Stark effect caused by in-plane electrical fields, the change in peak spectrum[30] here is due to the tunneling current between the MoS_2 channel and P^{++} Si. Fig. 3e compares the PL spectrum intensity of the QT-MoS_2 device and a control device without tunneling effects, both measured at a fixed $V_{DS} = 0$ V. The PL spectrum was measured across the V_{GS} range of −4 to 4 V, and the changes in the PL peak signal between $V_{GS} = 0$ and −4 V were compared. The normal device showed a variation rate of approximately 4.8%, while the leaky device with quantum tunneling exhibited a change rate of up to 71%. This significant difference in the PL optical measurements further confirms that the tunneling effect is the primary reason for the change in PL spectrum intensity with bias. Fig. 3f and g show the relationship between photocurrent I_{DS} and PL wavelength and peak intensity, respectively. It can be observed that when $V_{GS} < 0$ V, the photocurrent can reach 10^{-6} A, and due to the increase in hole concentration from quantum tunneling, the energy increases, causing the wavelength to shift towards the blue (blue shift), indicating a p-type doping effect in MoS_2. Another noteworthy observation is that, under positive gate bias ($V_{GS} > 0$ V), the photocurrent can also increase to the microampere level, similar to conventional MoS_2 photodetectors. However, unlike the case when $V_{GS} < 0$ V, the PL intensity and emission wavelength exhibit much less variation under positive bias.

Fig. S3 shows the behavior of the other three QT-MoS_2 FETs. While some variation in current density is observed—likely due to differences in internal defect densities of the as-grown MoS_2 flakes and minor variations in device morphology—the key features highlighted in our study remain consistent across all samples. Notably, each device demonstrates a significant increase in I_{DS} under negative gate bias ($V_{GS} < 0$) due to photoinduced tunneling current, as well as an enhancement in PL intensity and a discernible blue shift in the emission peak position, consistent with the trends shown in Fig. 1c, e and 3c. These results further confirm the robustness and repeatability of our findings.

The relationship between photocurrent I_{DS} and PL wavelength and peak intensity of thenormal MoS_2 FET device are shown in Fig. S4a and b, respectively. Compared to the QT-MoS_2 FET, the normal MoS_2 FET exhibits no significant variation in either the PL peak position or PL peak intensity under different applied V_{GS}. This observation suggests that the changes in the PL spectrum in the QT-MoS_2 FET are predominantly driven by the tunneling mechanism. Fig. S5 presents PL spectra for the normal MoS_2 FET at higher V_{GS} range from +20 V to −55 V. We observe a slight blue shift in peak position when $V_{GS} < -40$ V, with a maximum shift of ∼4 nm. The QT-MoS_2 FET demonstrated a more substantial shift of ∼12 nm as V_{GS} was swept from +4 V to −4 V (Fig. 3f), confirming that tunneling-induced PL spectrum variation is more efficient in the quantum tunneling configuration. Fig. S6 presents time-resolved characteristics for the QT-MoS_2 FET. The results indicate that the QT-MoS_2 FET maintains reliable PL response and tunneling current characteristics even under repeated electrical and optical measurement. Fig. S7 illustrates the bias stress characteristics of the QT-MoS_2 FET. The results demonstrate that the device exhibits robust bias stress stability, even under stringent conditions.

To elucidate the observed spectral changes, the energy band diagram of the QT-MoS_2 FET under varying gate–source voltages (V_{GS}) is illustrated in Fig. 4a. When a negative V_{GS} is applied to the MoS_2 channel under 532 nm laser illumination, a significant number of holes in the valence band are photo-excited, allowing them to tunnel through the SiO_2/hBN layer into the P^{++} Si gate electrode, thereby generating a photocurrent. The tunneling process can lead to the filling of trap states or defect states in the MoS_2. By passivating these defects, the tunneling current reduces non-radiative recombination pathways. This allows more excitons to recombine radiatively, thereby enhancing the PL intensity of the A exciton. On the other hand, to maintain charge neutrality within the MoS_2 channel, free electrons from P^{++} Si also inject into the MoS_2 channel region and effect the nonequilibrium electron population to create trions.[36,37] Fig. 4b presents the Lorentzian fits of the MoS_2 channel's PL spectrum at V_{GS} = −6 V, highlighting contributions from A excitons (622 nm), B excitons (673 nm), trions (710 nm), and defect-related peaks (751 nm). The PL spectrum was deconvoluted into these four components, with the A-exciton peak dominating. Fig. 4c and d depict the dependence of A-exciton, B-exciton, and trion peak intensities on varying V_{GS} values. Notably, higher A-exciton and trion intensities were observed under more negative V_{GS} conditions, indicating stronger radiative recombination as the photocurrent increases. The lower B/A ratio reflects the reduced trap density in the MoS_2 channel, which can be attributed to free carriers from P^{++}Si filling the trap states.[38] Fig. S8 presents the time-resolved photocurrent (*I–T*) property conducted under various laser intensities and following the responsivity and specific detectivity. The extracted responsivity and detectivity are approximately 0.3 A W^{-1} and 10^{10} Jones, respectively. These values indicate a relatively low level of photoresponse, primarily attributed to the high defect density within the gate dielectric layer compared to other high-performance 2D base photodetector.[39–41] Since that

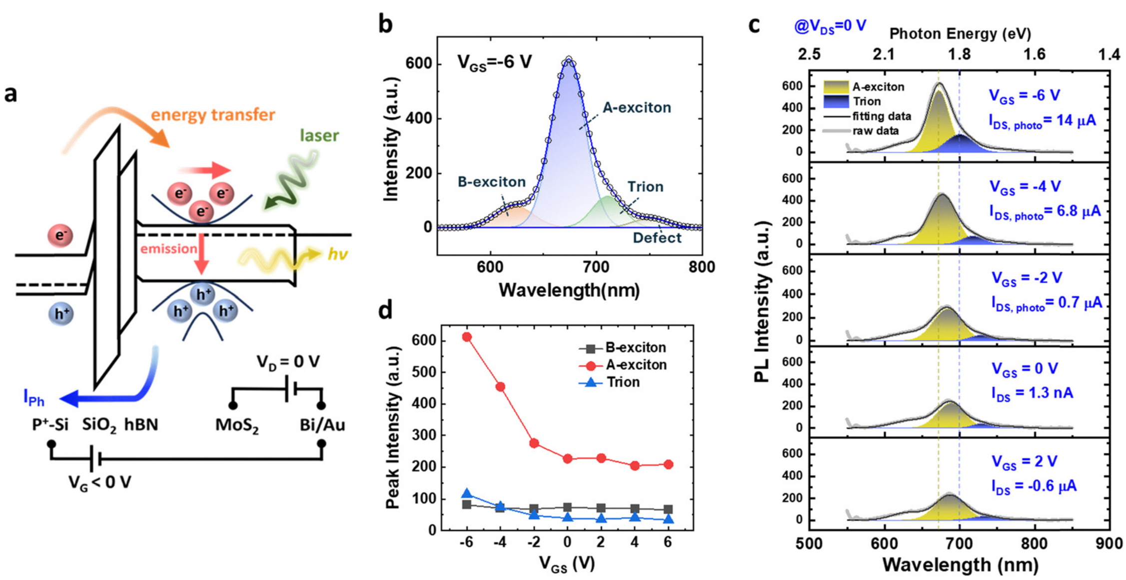

Fig. 4 Exciton and trion dissociation properties of the QT-MoS_2 FET under varying gate biases. (a) Energy band diagram of the QT-MoS_2 FET under 532 nm laser illumination. (b) PL spectrum showing the A exciton, trion, and B exciton in the QT-MoS_2 FET channel at V_{DS} = 0 V and V_{GS} = −6 V. (c) PL spectrum evolution with applied V_{GS}. The PL spectra in (b) and (c) were obtained by fitting the experimental data using the Gaussian function. (d) Peak intensities of the A exciton, trion, and B exciton in the PL spectra as a function of the applied V_{GS}.

achieving high responsivity and detectivity could significantly enhance the applicability of excitonic electronics, we suggest that the as engineering 2D material heterostructures or plasmonic structure could improve the device's photodetection capabilities.[42,43]

Summary

In conclusion, we have demonstrated the optoelectronic properties of QT-MoS_2 FETs fabricated on a high trap density gate oxide layer. The devices were designed to exhibit TA tunneling photocurrents, enabling the exploration of PL spectra variations in MoS_2 channels under different applied V_{GS}. The results reveal the formation of A and B excitons, and trions, and defect-related peaks in the MoS_2 monolayer, where TA tunneling currents enhance the optical response. Through comparative analysis with normal MoS_2 FETs, we demonstrate that the PL intensity changes in QT-MoS_2 FETs are attributed to the tunneling current between the MoS_2 channel and P^{++} Si gate, differing from typical exciton modulation by gate-induced doping. These results provide insights into the fundamental carrier dynamics and excitonic behavior in 2D material-based optoelectronic devices, offering potential for their application in next-generation sensors, light emitting diodes and photodetectors.

Method

Synthesis details of MoS_2

Monolayer MoS_2 flakes were synthesized on *c*-plane sapphire substrates *via* atmospheric-pressure chemical vapor deposition (APCVD). The process was conducted in a 3-inch quartz tube furnace equipped with three independently controlled heating zones. High-purity molybdenum trioxide (MoO_3, 99.99%, Sigma-Aldrich) was placed in a quartz crucible located in the central heating zone, while the sapphire substrates were positioned face-down on an adjacent crucible next to the MoO_3 source. Elemental sulfur (S, 99.99%, Sigma-Aldrich) was placed in a third crucible at the upstream (inlet) zone of the furnace. The synthesis was carried out at 800 °C for 15 minutes under a constant flow of argon gas at 300 sccm, serving as the carrier medium. After the growth process, the system was allowed to cool naturally to room temperature.

Wet transfer process

The MoS_2 wet transfer process involved the use of poly(methyl methacrylate) (PMMA) as a supporting film to detach MoS_2 flakes from the SiO_2 substrate. Firstly, PMMA was spin-coated onto the MoS_2 samples at 4000 rpm for 90 s, followed by baking at 110 °C for 3 min to remove residual moisture and promote cross-linking of the PMMA chains, thereby strengthening the mechanical integrity of the support layer and minimizing tearing during delamination. Subsequently, the edge of the PMMA film was carefully scribed with a blade, and the film was then slowly immersed into an 80 °C 1 M KOH solution. After soaking for less than 30 minutes, the PMMA film, carrying the MoS_2 samples, could be easily peeled off. Before transferring it onto the destination substrate, the floating PMMA/MoS_2 film was rinsed several times with deionized water. Finally, baking at 110 °C for 1 hour was performed to reduce air gaps or trapped solvents at the interface and to improve adhesion between the MoS_2 and the hBN/SiO_2/P^{++} Si substrate. The PMMA film was removed using acetone.

Author contributions

The device fabrication was performed by Ruei-Yu Hsu and You-Jia Huang. The measurements were conducted by Bor-Wei Liang, Ruei-Yu Hsu, and Ye-Ru Chen. The data analysis was provided by Bor-Wei Liang and Ruei-Yu Hsu. This manuscript was prepared by Bor-Wei Liang and Ruei-Yu Hsu. This manuscript was reviewed by Chin-Yuan Su, Ting-Hua Lu, and Yann-Wen Lan, and was finalized by Yann-Wen Lan. This project was supervised by Bor-Wei Liang and Yann-Wen Lan.

Conflicts of interest

The authors declare no competing interests.

Data availability

The data supporting this article have been included as part of the SI. Supplementary information available: Fig. S1. AFM image and Raman spectra of the monolayer MoS_2. Fig. S2. Transfer characteristics (I_{DS}–V_{GS}) with and without the hBN layer. Fig. S3. Characterization of three additional QT-MoS_2 FET devices. Fig. S4. Photocurrent (IDS, photo) and PL peak of a normal MoS_2 FET. Fig. S5. PL spectra of the normal MoS_2 FET under different VGS ranges. Fig. S6. Time-resolved IDS and PL spectra of the QT-MoS_2 FET. Fig. S7. Bias stress measurements of the QT-MoS_2 FET. Fig. S8. Power-dependent photocurrent, responsivity, and detectivity of QT-MoS_2 FET devices. See DOI: https://doi.org/10.1039/d5nh00089k

Acknowledgements

This work was supported by National Science and Technology Council, Taiwan (113-2112-M-003-017-MY3 (Bor-Wei Liang), 111-2628-M-003-002-MY3 (Yann-Wen Lan)). This work was also in part supported by the Taiwan Semiconductor Research Institute (JDP114-Y1-054), National Synchrotron Radiation Research Center, the Semiconductor Fabrication Lab of the Consortia of Key Technologies, and the Nano-Electro-Mechanical-System Research Center, National Taiwan University.

References

1 P.-C. Shen, *et al.*, Ultralow contact resistance between semimetal and monolayer semiconductors, *Nature*, 2021, **593**, 211–217.

2 S. Das, *et al.*, Transistors based on two-dimensional materials for future integrated circuits, *Nat. Electron.*, 2021, **4**, 786–799.

3 B. Radisavljevic, M. B. Whitwick and A. Kis, Integrated circuits and logic operations based on single-layer MoS2, *ACS Nano*, 2011, **5**, 9934–9938.
4 J. Tang, *et al.*, Low power flexible monolayer MoS2 integrated circuits, *Nat. Commun.*, 2023, **14**, 3633.
5 Y. Lin, *et al.*, Dielectric screening of excitons and trions in single-layer MoS2, *Nano Lett.*, 2014, **14**, 5569–5576.
6 T. G. Pedersen, Exciton Stark shift and electroabsorption in monolayer transition-metal dichalcogenides, *Phys. Rev. B*, 2016, **94**, 125424.
7 D. Basov, M. Fogler and F. García de Abajo, Polaritons in van der Waals materials, *Science*, 2016, **354**, aag1992.
8 C. C. Price, N. C. Frey, D. Jariwala and V. B. Shenoy, Engineering zero-dimensional quantum confinement in transition-metal dichalcogenide heterostructures, *ACS Nano*, 2019, **13**, 8303–8311.
9 G. A. Ermolaev, *et al.*, Broadband optical properties of monolayer and bulk MoS2, *npj 2D Mater. Appl.*, 2020, **4**, 21.
10 Z. Hu, *et al.*, Energy transfer driven brightening of MoS2 by ultrafast polariton relaxation in microcavity MoS2/hBN/WS2 heterostructures, *Nat. Commun.*, 2024, **15**, 1747.
11 C. Mai, *et al.*, Many-body effects in valleytronics: direct measurement of valley lifetimes in single-layer MoS2, *Nano Lett.*, 2014, **14**, 202–206.
12 X. Xu, W. Yao, D. Xiao and T. F. Heinz, Spin and pseudospins in layered transition metal dichalcogenides, *Nat. Phys.*, 2014, **10**, 343–350, DOI: **10.1038/nphys2942**.
13 L. Ren, Exciton and spin-valley properties in WSe_2 monolayers, INSA de Toulouse, PhD thesis, University of Toulouse, 2023.
14 J.-H. Kang, *et al.*, Monolithic 3D integration of 2D materials-based electronics towards ultimate edge computing solutions, *Nat. Mater.*, 2023, **22**, 1470–1477.
15 H. Kum, *et al.*, Epitaxial growth and layer-transfer techniques for heterogeneous integration of materials for electronic and photonic devices, *Nat. Electron.*, 2019, **2**, 439–450.
16 C. Tan, *et al.*, Electrically tunable interlayer recombination and tunneling behavior in WSe 2/MoS 2 heterostructure for broadband photodetector, *Nanoscale*, 2024, **16**, 6241–6248.
17 Y. Zhu, *et al.*, Non-volatile 2D MoS2/black phosphorus heterojunction photodiodes in the near-to mid-infrared region, *Nat. Commun.*, 2024, **15**, 6015.
18 T. Deng, *et al.*, Polarization-sensitive photodetectors based on three-dimensional molybdenum disulfide (MoS_2) field-effect transistors, *Nanophotonics*, 2020, **9**, 4719–4728.
19 Y. Gao, G. Zhou, H. K. Tsang and C. Shu, High-speed van der Waals heterostructure tunneling photodiodes integrated on silicon nitride waveguides, *Optica*, 2019, **6**, 514–517.
20 C. Liu, *et al.*, Realizing the switching of optoelectronic memory and ultrafast detector in functionalized-black phosphorus/MoS2 heterojunction, *Laser Photonics Rev.*, 2023, **17**, 2200486.
21 P. HL, P. Mondal, A. Bid and J. K. Basu, Electrical and chemical tuning of exciton lifetime in monolayer MoS2 for field-effect transistors, *ACS Appl. Nano Mater.*, 2019, **3**, 641–647.
22 A. Newaz, *et al.*, Electrical control of optical properties of monolayer MoS2, *Solid State Commun.*, 2013, **155**, 49–52.
23 X. Zhang, *et al.*, Shape-uniform, high-quality monolayered MoS2 crystals for gate-tunable photoluminescence, *ACS Appl. Mater. Interfaces*, 2017, **9**, 42121–42130.
24 W. Zheng, *et al.*, Light emission properties of 2D transition metal dichalcogenides: fundamentals and applications, *Adv. Opt. Mater.*, 2018, **6**, 1800420.
25 A. Pospischil and T. Mueller, Optoelectronic devices based on atomically thin transition metal dichalcogenides, *Appl. Sci.*, 2016, **6**, 78.
26 C. Gong, *et al.*, Electronic and optoelectronic applications based on 2D novel anisotropic transition metal dichalcogenides, *Adv. Sci.*, 2017, **4**, 1700231.
27 X. Zhou, *et al.*, 2D layered material-based van der Waals heterostructures for optoelectronics, *Adv. Funct. Mater.*, 2018, **28**, 1706587.
28 K. S. Kim, *et al.*, The future of two-dimensional semiconductors beyond Moore's law, *Nat. Nanotechnol.*, 2024, **19**, 895–906.
29 J. W. John, A. Mishra, R. Debbarma, I. Verzhbitskiy and K. E. J. Goh, Probing charge traps at the 2D semiconductor/dielectric interface, *Nanoscale*, 2023, **15**, 16818–16835.
30 M. Massicotte, *et al.*, Dissociation of two-dimensional excitons in monolayer WSe2, *Nat. Commun.*, 2018, **9**, 1633.
31 S. Haastrup, S. Latini, K. Bolotin and K. S. Thygesen, Stark shift and electric-field-induced dissociation of excitons in monolayer MoS 2 and h BN/MoS 2 heterostructures, *Phys. Rev. B*, 2016, **94**, 041401.
32 B. Scharf, *et al.*, Excitonic Stark effect in MoS_2 monolayers, *Phys. Rev. B*, 2016, **94**, 245434.
33 H. Lee, *et al.*, Quantum tunneling high-speed nano-excitonic modulator, *Nat. Commun.*, 2024, **15**, 8725.
34 A. Pelella, *et al.*, Graphene–silicon device for visible and infrared photodetection, *ACS Appl. Mater. Interfaces*, 2021, **13**, 47895–47903.
35 M. P. Houng, Y. H. Wang and W. J. Chang, Current transport mechanism in trapped oxides: A generalized trap-assisted tunneling model, *J. Appl. Phys.*, 1999, **86**, 1488–1491.
36 S. Golovynskyi, *et al.*, Trion binding energy variation on photoluminescence excitation energy and power during direct to indirect bandgap crossover in monolayer and few-layer MoS2, *J. Phys. Chem. C*, 2021, **125**, 17806–17819.
37 Y. Ma, R. A. Kalt and A. Stemmer, Local strain and tunneling current modulate excitonic luminescence in MoS 2 monolayers, *RSC Adv.*, 2022, **12**, 24922–24929.
38 K. M. McCreary, A. T. Hanbicki, S. V. Sivaram and B. T. Jonker, A-and B-exciton photoluminescence intensity ratio as a measure of sample quality for transition metal dichalcogenide monolayers, *APL Mater.*, 2018, **6**, 111106.
39 C.-Y. Huang, *et al.*, Hybrid 2D/3D MoS2/GaN heterostructures for dual functional photoresponse, *Appl. Phys. Lett.*, 2018, **112**, 233106.

40 M. Moun, M. Kumar, M. Garg, R. Pathak and R. Singh, Understanding of MoS2/GaN heterojunction diode and its photodetection properties, *Sci. Rep.*, 2018, **8**, 11799.
41 H. S. Nalwa, A review of molybdenum disulfide (MoS 2) based photodetectors: from ultra-broadband, self-powered to flexible devices, *RSC Adv.*, 2020, **10**, 30529–30602.
42 D. Akinwande, *et al.*, Graphene and two-dimensional materials for silicon technology, *Nature*, 2019, **573**, 507–518, DOI: 10.1038/s41586-019-1573-9.
43 H.-Y. Lan, *et al.*, Gate-tunable plasmon-enhanced photodetection in a monolayer MoS2 phototransistor with ultrahigh photoresponsivity, *Nano Lett.*, 2021, **21**, 3083–3091.

